Electronic Supplementary Material

Bimetallic reduced graphene oxide/zeolitic imidazolate framework hybrid aerogels for efficient heavy metals removal

Nurul A. Mazlan, Allana Lewis, Fraz Saeed Butt, Rajakumari Krishnamoorthi, Siyu Chen, Yi Huang **(✉)**

School of Engineering, Institute for Materials & Processes, The University of Edinburgh, Edinburgh EH9 3FB, UK

E-mail: Yi.Huang@ed.ac.uk

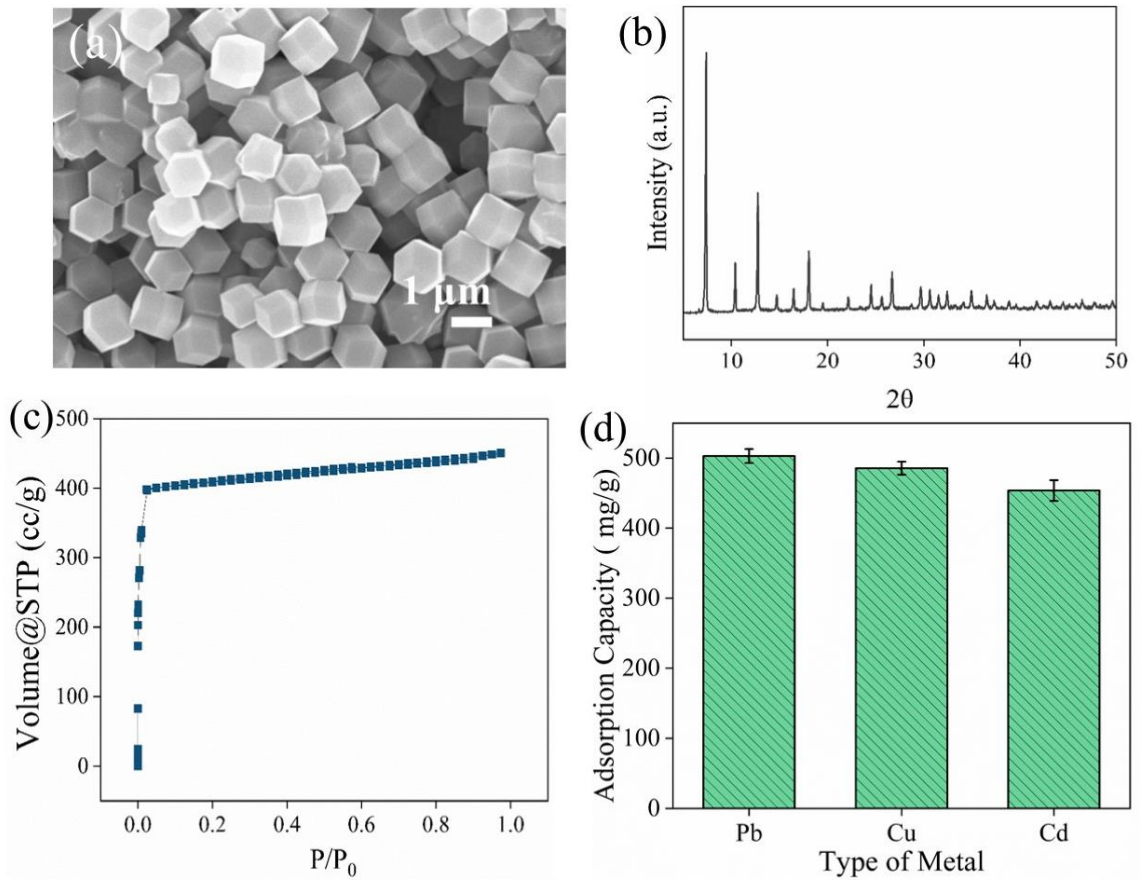

Figure S1. Characterization and performance of ZIF-8; (a) SEM images; (b) XRD pattern ; (c) BET and (d) Adsorption performance of heavy metals.

Fig. S1 presented the characterization of ZIF-8 material and the adsorption performance towards various heavy metals. **Fig. S1a** showed the morphology of the nanosized ZIF-8 crystals, revealing a polyhedral structure. **Fig. S1b** displayed the XRD pattern of the ZIF-8 powders, which resembled the reported ZIF-8 pattern in the literature confirming the high purity of the sample [1]. The N_2 sorption isotherm (**Fig. S1c**) revealed a type I isotherm, with a calculated specific BET surface area of 1287 m^2/g [1]. **Fig. S2d** presented the adsorption of Pb^{2+}, Cu^{2+}, and Cd^{2+} by ZIF-8 nanocrystals with an initial concentration of 200 mg g at pH 6. The ZIF-8 exhibited an adsorption capacity of 503 ± 9.9 mg/g, 485 ± 9.3 mg/g, and 453 ± 14.8 mg/g for Pb^{2+}, Cu^{2+}, and Cd^{2+}, respectively.

The high-resolution scans of C 1s, O 1s, N 1s, Zn 2p, and Co 2p are shown in **Fig. S2b–f.** As shown in **Fig. S2b**, the high-resolution spectrum of C 1s for the rGO samples can be analyzed with three peaks positioned at 284.8 eV, 286.3 eV, and 288.4 eV, which are associated with C–C, C–O, and O–C=O bonds, respectively. A notable alteration of peaks was observed after PDA functionalization, where a new peak positioned at 286.1 eV associated with the C–N component was observed. The spectrum can be deconvoluted into five peaks at 284.6 eV, 286.1 eV, 287.1 eV, 288.7 eV, and 291.5 eV, respectively, indicating C–C, C–O/C–N, C=O/C=N, O–C=O, and π-π* bonds in the spectra [2]. The appearance of the π-π* 'shake-up' peak originating from the aromatic rings of PDA implied that π-π*stacking could potentially be one of the interaction modes involved in the wrapping/coating of PDA on the surface of

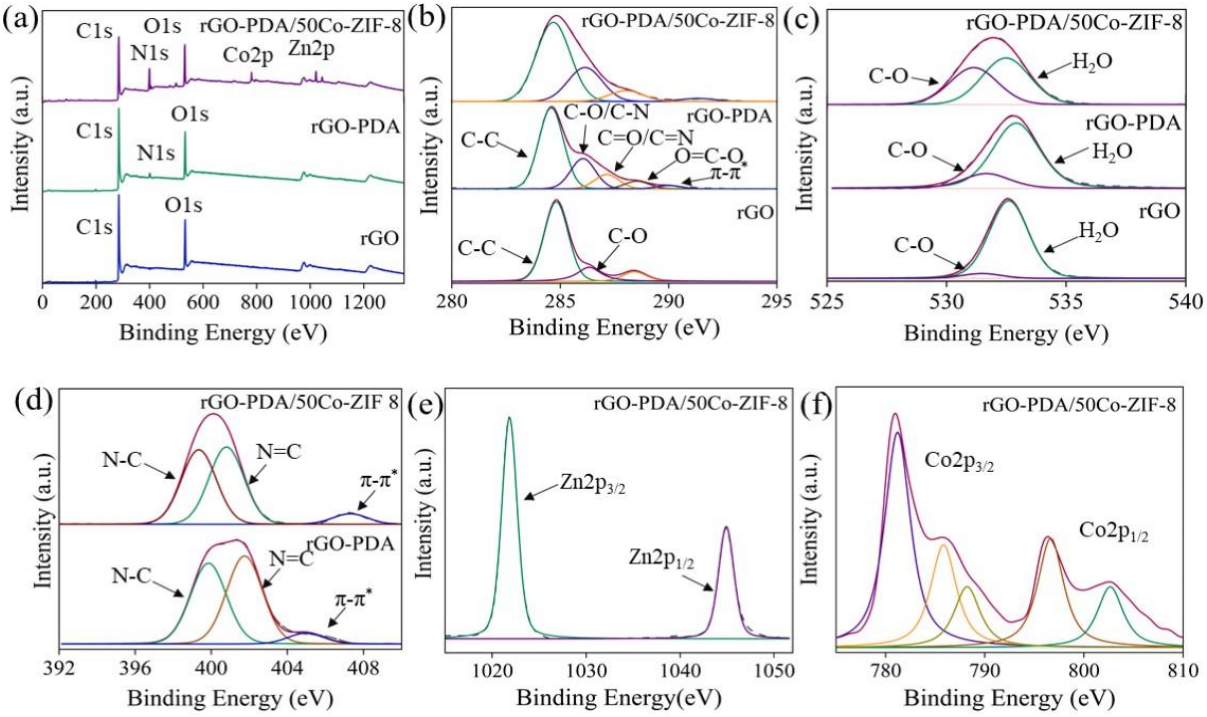

Figure S2. XPS analysis of rGO, rGO-PDA and rGO-PDA/50Co-ZIF-8 aerogels: (a) full spectra; (b) C1s spectra; (c) O1s spectra (d) N1s spectra; (e) Zn 2p spectra; and (f) Co 2p spectra.

the rGO aerogel. A significant change was observed in the high-resolution C 1s spectrum after the *in-situ* growth of Co-ZIF-8. The enhancement in the C–O/C–N peak and the disappearance of the O–C=O peak indicated the successful incorporation of Co-ZIF-8 into the structure. **Fig. S2c** revealed the O 1s spectrum for rGO, rGO-PDA, and rGO-PDA/50Co-ZIF-8 samples. The O 1s spectrum of rGO can be resolved into two peak components attributed to C–O and O–H positioned at 531.5 eV and 532.6 eV, respectively [3]. Likewise, the O 1s spectrum of the rGO-PDA presented the emergence of two peaks positioned at 531.6 eV and 532.8 eV which correspond to the C–O and O–H, respectively. Additionally, a notable increase in the C-O peak was observed due to the presence of the catechol group in the PDA structure. Meanwhile, the rGO-PDA/50Co-ZIF-8 aerogel displayed a notable increase in the peak component of oxygen positioned at 531.1 eV due to the presence of both Zn–O–N and Co–O–N peak components which have a binding energy of 529 eV – 531 eV [4,5]. The emergence of the Zn–O–N and Co–O–N bonds further demonstrated the efficacy of integrating rGO-PDA aerogels with Co-ZIF-8 crystals, thereby imparting improved mechanical stability to the material. Finally, **Fig. S2d** revealed the N 1s spectrum at binding energy ~399.0 for rGO-PDA and rGO-PDA/50Co-ZIF-8 samples. The

rGO-PDA sample exhibited two distinct peak components at binding energy 399.8 eV and 401.6 eV associated with the primary and secondary amines groups which belong to the heterocycle of PDA, respectively [6]. The small peak that was shifted several eV from the main nitrogen peak at 405.0 eV is due to the presence of π-π^* satellite features within the nitrogen-containing peak [7]. The high-resolution N 1s spectrum for the rGO-PDA/50Co-ZIF-8 aerogel revealed two prominent peaks corresponding to N–C and N=C, positioned at 398.9 eV and 400.3 eV, respectively. These peaks are attributed to the presence of Co-ZIF-8 and the combination of Co-ZIF-8 with rGO-PDA, respectively. It is important to highlight that the attribution of the N–C bond is associated with the imidazole group present in the Co-ZIF-8 crystals [8]. The Zn and Co spectra were only observed for the rGO-PDA/Co-ZIF-8 aerogel. As depicted in **Fig. S2e,** the Zn 2p spectrum revealed two prominent peaks positioned at binding energy 1045.1 eV and 1021.9 eV which are associated with Zn $2p_{1/2}$ and Zn $2p_{3/2}$, respectively [9]. Meanwhile, the Co 2p spectrum exhibited two main peaks attributed to the Co $2p_{3/2}$ and Co $2p_{1/2,}$ at binding energies of 781.3 eV and 796.3 eV, respectively (refer to **Fig. S2f**) [10].

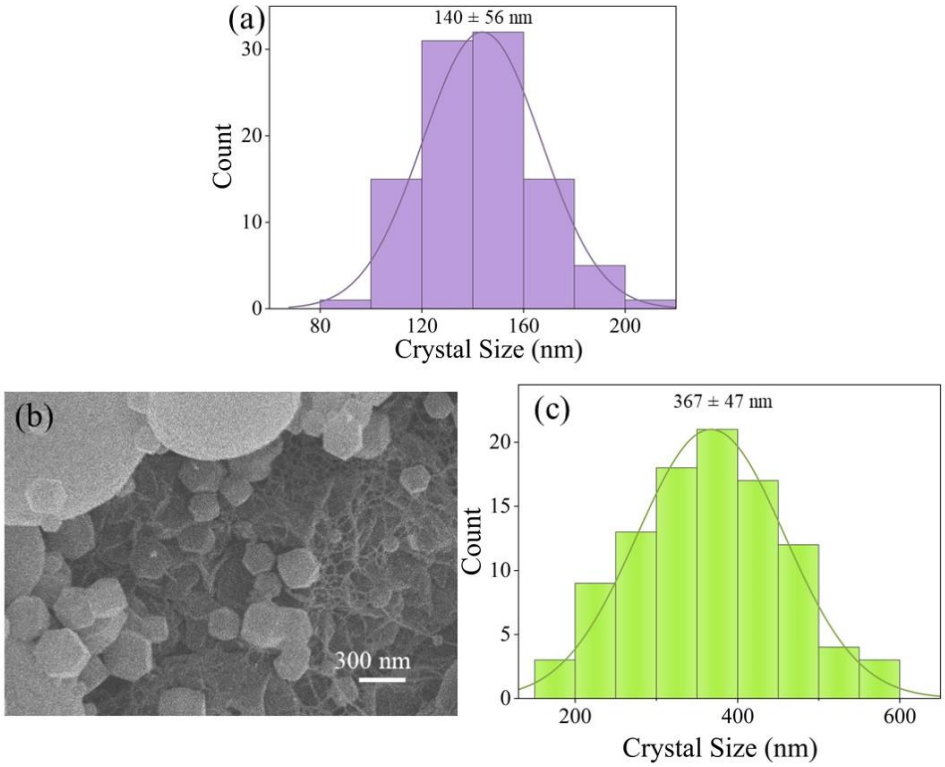

Figure S3. Microstructure of the as-synthesised aerogels: (a) Particle size distribution of rGO-PDA/ZIF-8 aerogel; (b) SEM imaging; and (c) Crystal size distribution on the surface of rGO-PDA/ZIF-

Fig. S3 displayed the SEM images of the nanocrystals nanocrystals with 100% cobalt crystals decorated on the rGO-PDA aerogel. The crystal size was measured using ImageJ software to analyze the effect of cobalt doping level on the crystal growth. The crystals exhibit a bigger crystal size with a crystal size distribution of 367 ± 47 nm compared to cobalt-doped crystals.

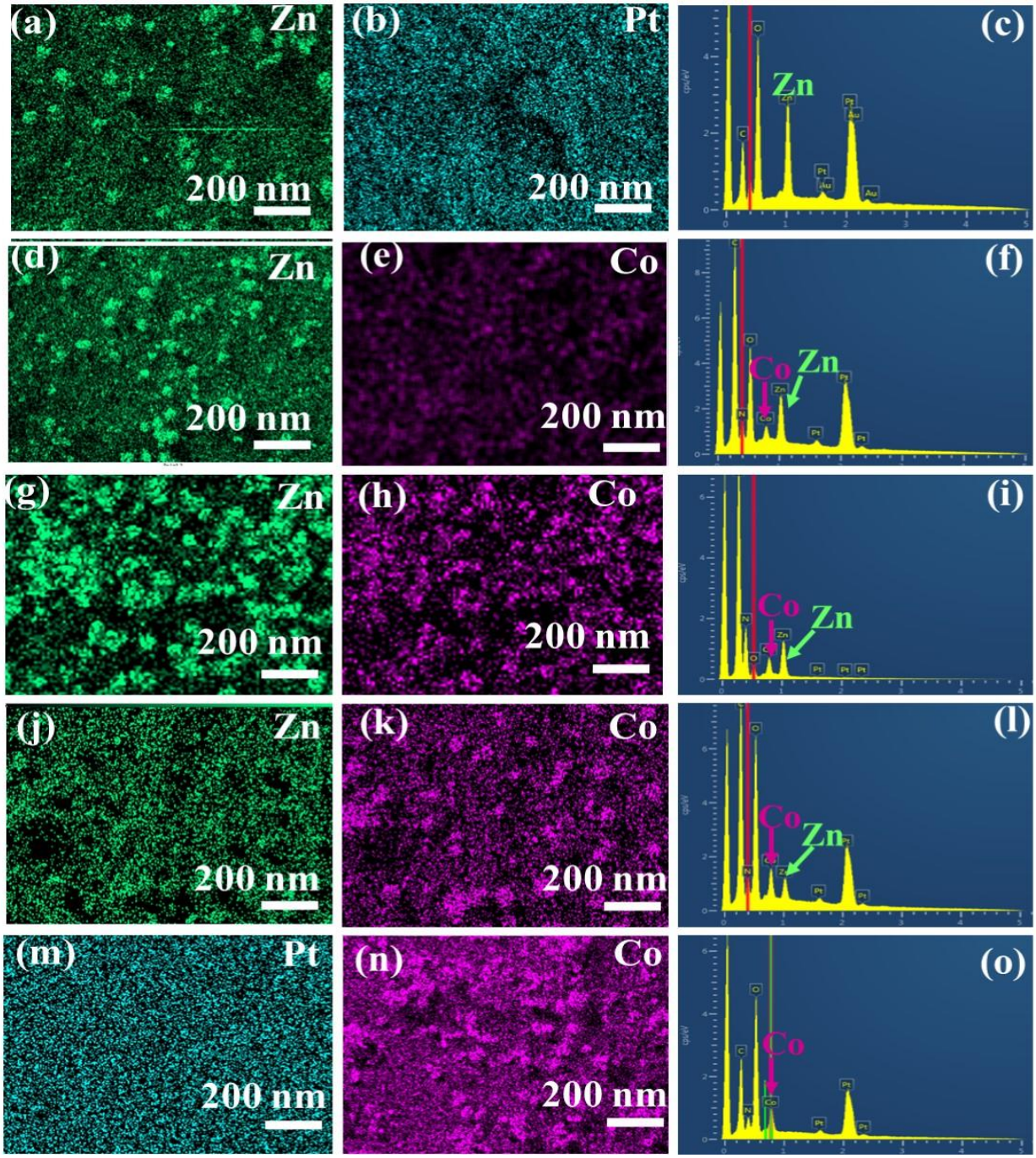

Figure S4. EDS mapping of platinum, cobalt and zinc, and EDX spectra for as-synthesized aerogel at different cobalt concentrations: (a–c) rGO-PDA/ZIF-8; (d–f) rGO-PDA/30Co-ZIF-8; (g–i) rGO-PDA/50Co-ZIF-8; (j–l) rGO-PDA/70Co-ZIF-8; and (m–o) rGO-PDA/ZIF-67.

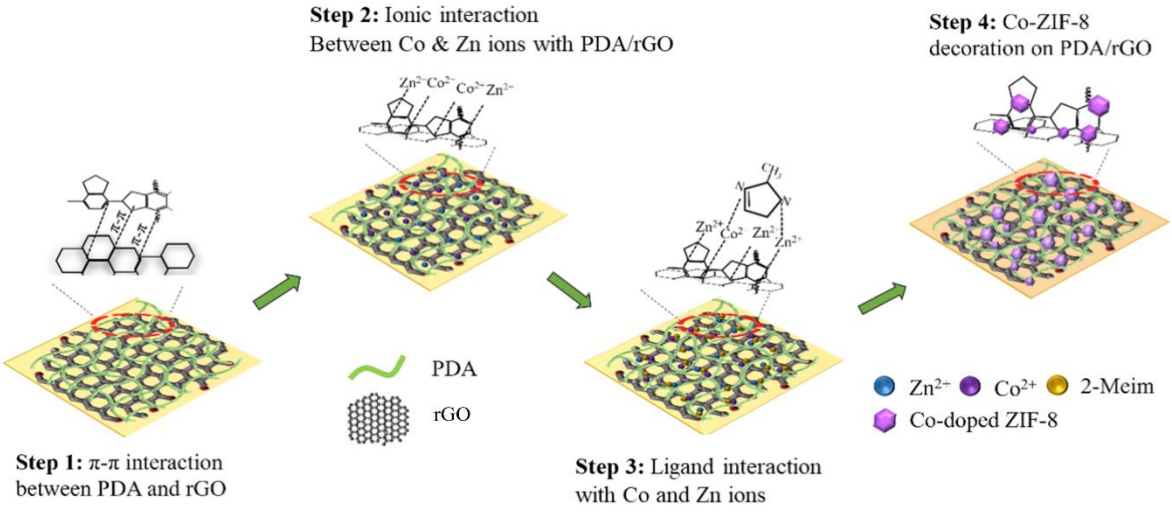

Figure S5. Illustration of the rGO-PDA/Co-ZIF-8 aerogel formation mechanism.

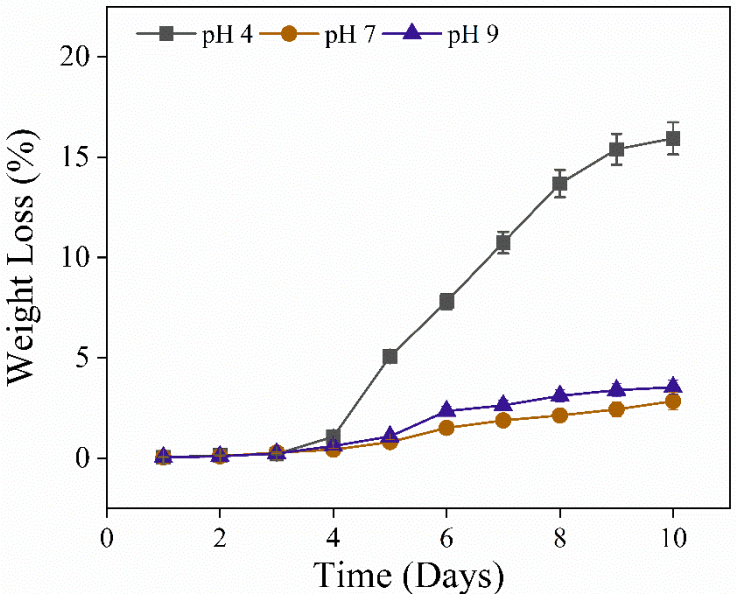

Figure S6. Degradation of the rGO-PDA/50Co-ZIF-8 aerogel at different pH levels.

Fig. S6 presented the degradation of the rGO-PDA/50Co-ZIF-8 aerogel at different pH for ten days. The aerogel exhibited the highest degradation at pH 4 with a mass loss of ~ 15%. This is due to the destabilization of polydopamine and the dissolution of ZIF crystals in acidic conditions[11][12]. The aerogels demonstrated good stability at both pH 7 and pH 9, with only a marginal mass loss of approximately 2-3%.

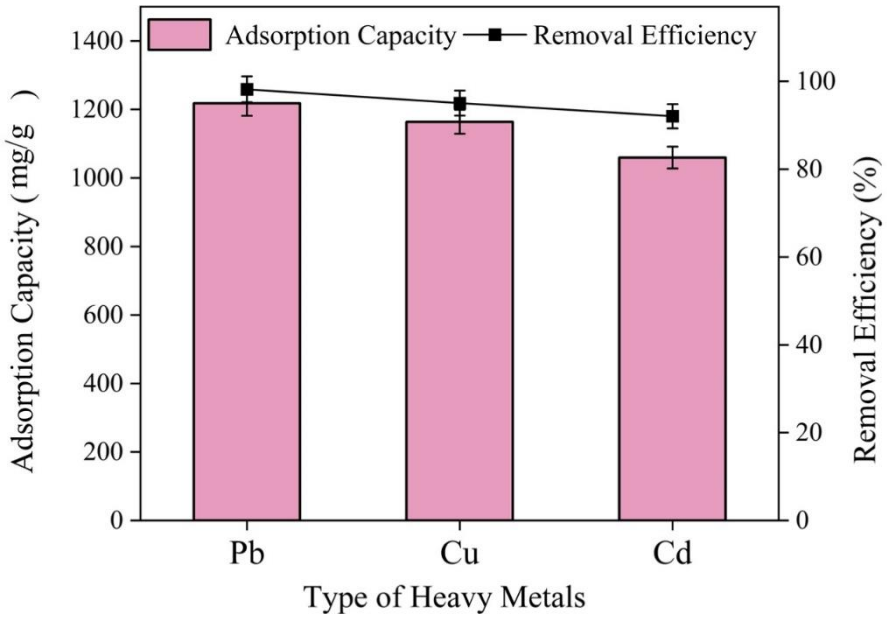

Figure S7. rGO-PDA/50Co-ZIF-8 aerogel adsorption performance for different types of heavy metals.

The adsorption capacity (mg g^{-1}) and removal efficiency (%) of the rGO-PDA/50Co-ZIF-8 aerogel were examined for different types of heavy metals with an initial concentration of 0.6 mmol L^{-1} **(Fig. S7).** The aerogels showed the highest adsorption capacity towards Pb (II), followed by Cu (II) and Cd (II). More specifically, the aerogel exhibits an adsorption capacity of 1213 ± 36.54 mg/g, 1162 ± 34.91 mg/g, and 1058 ± 31.77 mg/g for Pb (II), Cu (II), and Cd (II) respectively. Likewise, the aerogel showed the highest removal efficiency of 99 ± 2.94% for Pb (II), followed by Cu (II) and finally Cd (II), each having a removal efficiency of 95 ± 2.85% and 92 ± 2.76%, respectively. The interaction between the surface of rGO-PDA/30Co-ZIF-8 aerogel and the heavy metals is significantly influenced by the electronegativity of heavy metal ions [13]. Based on the Pauling scale of electronegativity [14], Pb (II) has the highest electronegativity of 2.33, which means the ions have a strong attraction to the surface of the aerogels and are thus easily adsorbed [15]. Cu (II) has a medium electronegativity of 1.90, followed by Cd (II) which has the lowest electronegativity value of 1.69 which reflects the adsorption performance of the aerogel towards these heavy metal ions [14]. Therefore, it can be concluded that greater electronegativity leads to greater adsorption capacity. This is because there is more attraction between two atoms when the electronegativity difference between nitrogen (or oxygen) and metal atoms is large.

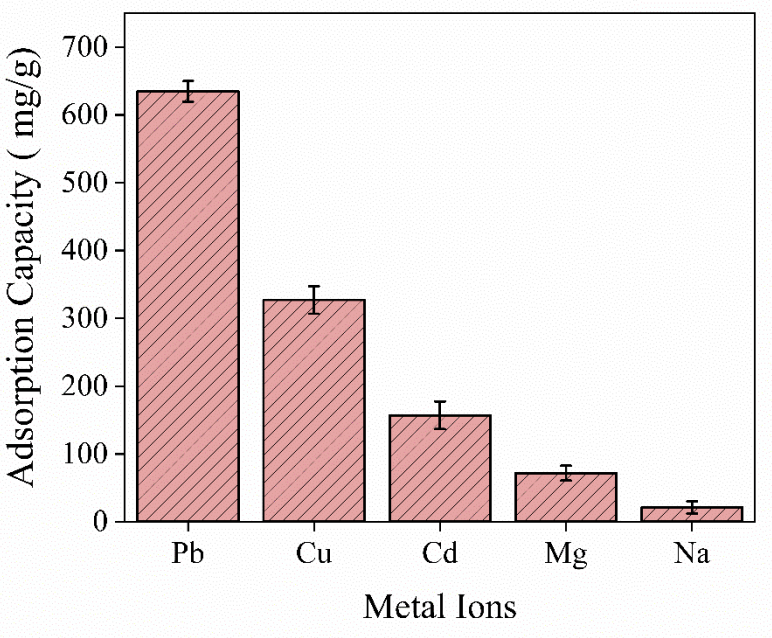

Figure S8. Adsorption selectivity of rGO-PDA/50Co-ZIF-8 aerogel

The ion selectivity of the rGO-PDA/Co-ZIF-8 aerogel was assessed by determining the adsorption capacity of the aerogel in a solution containing different heavy metals (**Fig. S8**). It was noted that the aerogel exhibited the highest adsorption capacity for Pb ions with an adsorption capacity of 634 ± 15.2 mg/g, followed by Cu, Cd, Mg, and Na with the adsorption capacity of 327 ± 20.4 mg/g, 156 ± 20.4 mg/g, 72 ± 10.8 mg/g, and 21 ± 8.9 mg/g, respectively. The total adsorption capacity of all the metals is 1211 ± 15.1 mg/g.

Table S1. Weight percentage (%) of the elements in the as-synthesized aerogels.

Aerogels	Weight%	
	Cobalt	Zinc
rGO-PDA/ZIF-8	0.00	21.00
rGO-PDA/30Co-ZIF-8	9.90	16.58
rGO-PDA/50Co-ZIF-8	13.63	13.67
rGO-PDA/70Co-ZIF-8	17.91	6.95
rGO-PDA/ZIF-67	23.95	0.00

Table S2. Comparison of BET surface for the as-synthesized aerogels

Aerogels	**Surface area (m^2/g)**
rGO-PDA/ZIF-8	855
rGO-PDA/30Co-ZIF-8	875
rGO-PDA/50Co-ZIF-8	900
rGO-PDA/70Co-ZIF-8	861
rGO-PDA/ZIF-67	815

Table S3. Isotherm constant for lead (Pb) adsorption

Adsorption models	Parameters	Estimated Values	Units
Langmuir's Isotherm	q_{max}	1241.0	mg/g
	K_L	3.2513	L/mg
	R^2	0.9998	---
Freundlich Isotherm	K_F	2.73×10^{-11}	mg/g
	1/n	1.9952	---
	R^2	0.7532	---

Table S4. Comparison of previously reported aerogel for heavy metal adsorption in aqueous media

Aerogels Materials	**Heavy Metals**	**q_{max} (mg/g)**	**Ref**
Sodium alginate/graphene oxide	Pb^{2+}, Cu^{2+},	267.4, 98.0	[16]
Sulfhydryl-modified chitosan	Cu^{2+}, Pb^{2+}, Cd^{2+},	81.1, 38.8, 38.1	[17]
Chitosan	Cu^{2+}	163.7	[18]
Biomass-based aerogel (CE/CSA)	Cu^{2+}	260.41	[19]
PDA-MMT/CS	Pb^{2+}, Cu^{2+},	475.61, 534.76	[20]
Fe_3O_4/CNF/PEI/SHMMT	Pb^{2+}, Cu^{2+}, Cd^{2+}	429.1, 381.7, 299.4	[21]
NFC/CS-5	Cr^{4+}	197.3	[22]
Cross-linked silica	Pd^{2+},	689.65	[23]
Cellulose/Graphene	Cu^{2+}, Cd^{2+} , Pb^{2+}	80.1, 102.2. 57.2	[24]
Polyaniline-modified hybrid Graphene	Pb^{2+}	185	[25]
Chitin/Chitosan	Cu^{2+}	59.2	[26]
ZIF-8@ALG-PEI	Pb^{2+}, Cd^{2+}	295.9, 249.8	[27]
Carboxylated-wood	Cu^{2+}	115	[28]
Schiff base (SCA-X)	Pb^{2+}, Cu^{2+},	357.1, 243.9	[29]
Ni/Co-MOF-CMC	Cu^{2+}	233.9	[30]
TMPA@MOF-801	Cr^{4+}	350.6	[31]
Mg-MOF-74@cellulose	Pb^{2+}, Cu^{2+}, Cd^{2+}	223.5, 74.3, 160.0	[32]
rGO-PDA/50Co-ZIF-8	**Pb^{2+}, Cu^{2+}, Cd^{2+}**	**1217.9, 1163.8, 1059.2**	**This work**

References

1. Lewis A, Butt FS, Wei X, Mazlan NA, Chen Z, Yang Y, Yang S, Radacsi N, Chen X, Huang Y. Crystallization and phase selection of zeolitic imidazolate frameworks in aqueous cosolvent systems: The role and impacts of organic solvents. Results in Engineering, 2023, 17: 100751

2. Nguyen DN, Sim U, Kim JK. Biopolymer-inspired N-doped nanocarbon using carbonized polydopamine: A high-performance electrocatalyst for hydrogen-evolution reaction. Polymers, 2020, 12(4): 912

3. Zangmeister RA, Morris TA, Tarlov MJ. Characterization of polydopamine thin films deposited at short times by autoxidation of dopamine. Langmuir, 2013, 29(27): 8619–8628

4. Liu Y, Fu J, He J, Wang B, He Y, Luo L, Wang L, Chen C, Shen F, Zhang Y. Synthesis of a superhydrophilic coral-like reduced graphene oxide aerogel and its application to pollutant capture in wastewater treatment. Chemical Engineering Science, 2022, 260: 117860

5. Zhu G, Li H, Deng S, Zhang C, Kang K, Zhang X, Li K. In situ growth of bimetallic Co/Zn-ZIF within wood scaffold for enhanced adsorption capacity and improved flame retardancy. Wood Science and Technology, 2022, 56(6): 1657–1673

6. Batul R, Bhave M, Mahon PJ, Yu A. Polydopamine nanosphere with in-situ loaded gentamicin and its antimicrobial activity. Molecules, 2020, 25(9): 2090

7. Khattak ZAK, Ahmad N, Younus HA, Ullah H, Yu B, Munawar KS, Ashfaq M, Ali S, Shahadat HM, Verpoort F. Synthesis of 3D cadmium(II)-carboxylate framework having potential for co-catalyst free CO_2 fixation to cyclic carbonates. Inorganics, 2022, 10(10): 162

8. Chen X, Qin L, Kang SZ, Li X. A special zinc metal-organic frameworks-controlled composite nanosensor for highly sensitive and stable SERS detection. Applied Surface Science, 2021, 550: 149302

9. Wu G, Zhou C, Li H, Xia S, Zhu Y, Han J, Xing W. Controlled fabrication of the biomass cellulose aerogel@ZIF-8 nanocomposite as efficient and recyclable adsorbents for methylene blue removal. Industrial Crops and Products, 2023, 193: 116169

10. Zhao M, Tesfay Reda A, Zhang D. Reduced Graphene Oxide/ZIF-67 Aerogel composite material for uranium adsorption in aqueous solutions. ACS Omega, 2020, 5(14): 8012–8022

11. Yang L, Wen J, Wang Q, Cui H. Effect of solution chemistry on the stability and transport of ZIF-8 in saturated porous media. Journal of Environmental Chemical Engineering, 2022, 10(3): 107562

12. Liu Q, Yu B, Ye W, Zhou F. Highly selective uptake and release of charged molecules by ph-responsive polydopamine microcapsules. Macromolecular bioscience, 2011, 11(9): 1227–1234.

13. Demir-Cakan R, Baccile N, Antonietti M, Titirici MM. Carboxylate-rich carbonaceous materials via one-step hydrothermal carbonization of glucose in the presence of acrylic acid. Chemistry of Materials, 2009, 21(3): 484–490

14. Kinraide TB, Yermiyahu U. A scale of metal ion binding strengths correlating with ionic charge, Pauling electronegativity, toxicity, and other physiological effects. Journal of inorganic biochemistry, 2007, 101(9): 1201–1213

15. Matos MPSR, Correia AAS, Rasteiro MG. Application of carbon nanotubes to immobilize heavy metals in contaminated soils. Journal of Nanoparticle Research, 2017, 19: 1–11

16. Jiao C, Xiong J, Tao J, Xu S, Zhang D, Lin H, Chen Y. Sodium alginate/graphene oxide aerogel with enhanced strength-toughness and its heavy metal adsorption study. International journal of biological macromolecules, 2016, 83:133–141

17. Zhang J, Wang Y, Liang D, Xiao Z, Xie Y, Li J. Sulfhydryl-modified chitosan aerogel for the adsorption of heavy metal ions and organic dyes. Industrial & Engineering Chemistry Research, 2020, 59(32): 14531–14536

18. Fan S, Chen J, Fan C, Chen G, Liu S, Zhou H, Liu R, Zhang Y, Hu H, Huang Z, et al. Fabrication of a CO2-responsive chitosan aerogel as an effective adsorbent for the adsorption and desorption of heavy metal ions. Journal of hazardous materials, 2021, 416: 126225

19. Liu Y, Ke Y, Shang Q, Yang X, Wang D, Liao G. Fabrication of multifunctional biomass-based aerogel with 3D hierarchical porous structure from waste reed for the synergetic adsorption of dyes and heavy metal ions. Chemical Engineering Journal, 2023, 451: 138934

20. Yuan M, Ye X, Song Z, Che L, Shang S, Yuan M, Wu S, Liu D, Cui S. A novel mussel-inspired layered montmorillonite-based composite aerogel for high-efficiency removal of heavy metal ions. Journal of Water Process Engineering, 2023, 54: 104075

21. Yuan M, Liu D, Shang S, Song Z, You Q, Huang L, Cui S. A novel magnetic Fe3O4/cellulose nanofiber/polyethyleneimine/thiol-modified montmorillonite aerogel for efficient removal of heavy metal ions: Adsorption behavior and mechanism study. International Journal of Biological Macromolecules, 2023, 253: 126634

22. Wang Q, Zuo W, Tian Y, Kong L, Cai G, Zhang H, Li L, Zhang J. An ultralight and flexible nanofibrillated cellulose/chitosan aerogel for efficient chromium removal: Adsorption-reduction process and mechanism. Chemosphere, 2023, 329: 138622

23. Parale VG, Choi H, Kim T, Phadtare VD, Dhavale RP, Lee KY, Panda A, Park HH. One pot synthesis of hybrid silica aerogels with improved mechanical properties and heavy metal adsorption: Synergistic effect of in situ epoxy-thiol polymerization and sol-gel process. Separation and Purification Technology, 2023, 308: 122934

24. Sun P, Wang M, Wu T, Guo L, Han W. Covalent crosslinking cellulose/graphene aerogels with high elasticity and adsorbability for heavy metal ions adsorption. Polymers, 2023, 15(11): 2434

25. Kuznetsova TS, Burakov AE, Burakova IV, Pasko TV, Dyachkova TP, Mkrtchyan ES, Memetova AE, Ananyeva OA, Shigabaeva GN, Galunin EV. Preparation of a polyaniline-modified hybrid graphene aerogel-like nanocomposite for efficient adsorption of heavy metal ions from aquatic media. Polymers, 2023, 15(5): 1101

26. Kuang J, Cai T, Dai J, Yao L, Liu F, Liu Y, Shu J, Fan J, Peng H. High strength chitin/chitosan-based aerogel with 3D hierarchically macro-meso-microporous structure for high-efficiency adsorption of Cu(II) ions and Congo red. International Journal of Biological Macromolecules, 2023, 230: 123238

27. Guo Z, Hou H, Zhou J, Wu X, Li Y, Hu L. Fabrication of novel 3D PEI-functionalized ZIF-8@alginate aerogel composites for efficient elimination of Pb(II) and Cd(II) from aqueous solution. Journal of Environmental Chemical Engineering, 2023, 11(5): 110446

28. He W, Cao J, Guo F, Guo Z, Zhou P, Wang R, Liang S, Pang Q, Wei B, Jiao Y, et al. Nanostructured carboxylated-wood aerogel membrane for high-efficiency removal of Cu (II) ions from wastewater. Chemical Engineering Journal, 2023, 468: 143747

29. Zhang Y, Yuan K, Magagnin L, Wu X, Jiang Z, Wang W. Schiff base functionalized silica aerogels for enhanced removal of Pb (II) and Cu (II): Performances, DFT calculations and LCA analysis. Chemical Engineering Journal, 2023, 462: 142019

30. Kong Q, Zhang H, Wang P, Lan Y, Ma W, Shi X. NiCo bimetallic and the corresponding monometallic organic frameworks loaded CMC aerogels for adsorbing Cu2+: Adsorption behavior and mechanism. International Journal of Biological Macromolecules, 2023, 244: 125169

31. Zhao J, He J, Liu L, Shi S, Guo H, Xie L, Chai X, Xu K, Du G, Zhang L. Self-cross-linking of metal-organic framework (MOF-801) in nanocellulose aerogel for efficient adsorption of Cr (VI) in water. Separation and Purification Technology, 2023, 327: 124942

32. Guo Z, Zhou J, Hou H, Wu X, Li Y. Recyclable Mg-MOF-74@cellulose aerogel composites for efficient removal of heavy metals from wastewater. Journal of Solid State Chemistry, 2023, 323: 124059